Journal of the European Ceramic Society 46 (2026) 117790

Contents lists available at ScienceDirect

Journal of the European Ceramic Society

journal homepage: www.elsevier.com/locate/jeurceramsoc

Magnesia-stabilized zirconia (MSZ) thermal barrier coatings by suspension plasma spraying: Coating properties and service life behavior

B.S. Constantino [a,b], Y.J. Sohn [a], G. Mauer [a,c,*]

[a] Forschungszentrum Jülich GmbH, Institute of Energy Materials and Devices, IMD-2: Materials Synthesis and Processing, Jülich 52425, Germany
[b] Universidade Federal do Oeste da Bahia, Centro Multidisciplinar de Bom Jesus da Lapa (CMBJL), Bom Jesus da Lapa 47600000, Brazil
[c] Technical University of Dortmund, Department of Mechanical Engineering, Dortmund 44227, Germany

ARTICLE INFO

Keywords:
Atmospheric plasma spray
Magnesia-stabilized zirconia
Pre oxidized coatings
Suspension plasma spray
Titanium oxide

ABSTRACT

Magnesia-stabilized zirconia (MSZ) coatings have low thermal conductivity and a high melting point. Currently, they are only indicated for use at lower temperatures than well-established yttria-stabilized zirconia (YSZ) coatings. This study investigated the life behavior of MSZ TBCs. The TBCs were prepared using two thermal spray technologies: atmospheric plasma spray (APS) and suspension plasma spray (SPS). The NiCoCrAlHfSi bond coat was pre-oxidized. The double-layer system, consisting of an APS intermediate layer of yttria-stabilized zirconia (YSZ) and an SPS top layer of MSZ, outperformed the single-layer MSZ APS and MSZ SPS pre-oxidized coatings. These results suggest that multi-layer coatings have the potential to improve MSZ coating performance. The influence of low-content titania doping was also investigated; however, no significant effect on the performance of the coatings was observed.

1. Introduction

Thermal barrier coatings (TBCs) are commonly used in extreme environments, such as in gas turbines for industrial and aerospace applications. TBCs are multilayer systems, consisting of a ceramic topcoat that act as an insulating layer, a thermally grown oxide (TGO) that forms as a result of high-temperature oxidation, and a bond coat that is sprayed onto the metallic substrate [1]. TBCs can provide significant protection against oxidation and corrosion at high temperatures [2] and can also increase component lifetime and operating temperature by reducing substrate temperature [3]. Therefore, TBCs should exhibit low thermal conductivity, phase stability, sintering resistance, a long thermal cycling life, and resistance to attack from calcia-magnesia-alumina-silica (CMAS) [4].

Yttria-stabilized zirconia (YSZ) has been the topcoat material of choice for the TBC industry [5–7]. However, many other materials have recently emerged as TBC candidates. For example, gadolinium zirconate (GZO) coatings have a high resistance to the CMAS environment [8,9]. YSZ coatings are compatible with the TGO at high temperatures, are tough, and are relatively easy to process [6]. As well known, yttria (Y_2O_3) stabilizes the non-transformable tetragonal phase (t') at high temperatures [10], which prevents from the undesirable phase transformation to the monoclinic zirconia phase during cooling. This transformation is accompanied by volume expansion, which can lead to failure [11–13]. Other components, such as calcia, ceria and magnesia, can also be used to produce alternative zirconia-stabilized ceramics [2,14,15].

To stabilize zirconia (ZrO_2), oxides must be doped into pure ZrO_2 materials. Cations with a radius greater than Zr^{4+} must be introduced into ZrO_2 lattices to replace some of the Zr^{4+} ions. Substitutional solid solutions then form, stabilizing the phase structure of the doped zirconia at room temperature and leading to a toughening effect [11]. Previous studies [16,17] have shown that incorporating ceria and titania (TiO_2) into zirconia enhances toughness and phase stability up to 1350°C. These properties are essential for the cyclic life and erosion resistance of TBCs. This enhancement is achieved by replacing Ti^{4+} with a larger Zr^{4+} cation, thereby increasing the tetragonality of the unit cell.

Magnesia-stabilized zirconia (MSZ) has desirable properties, including high resistance to thermal shock, low thermal conductivity, and creep resistance [15]. MSZ coatings (15–24 wt% MgO) are used in components with relatively low temperatures, such as the exhaust nozzles of jet engines, and are comparatively inexpensive [18]. However, few studies have focused on improving magnesia-stabilized zirconia thermal spray processing.

* Corresponding author at: Forschungszentrum Jülich GmbH, Institute of Energy Materials and Devices, IMD-2: Materials Synthesis and Processing, Jülich 52425, Germany.
E-mail address: g.mauer@fz-juelich.de (G. Mauer).

https://doi.org/10.1016/j.jeurceramsoc.2025.117790
Received 12 December 2024; Received in revised form 24 June 2025; Accepted 31 August 2025
Available online 2 September 2025

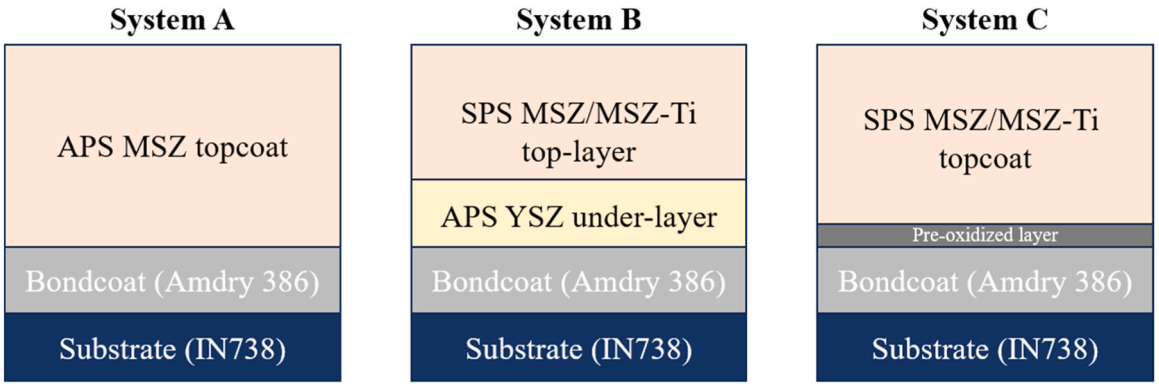

Fig. 1. Schematic diagram of (a) single-layered (system A), (b) bi-layered (system B) and (c) pre-oxidized (system C) coatings.

Ahmaniemi et al. [19] studied 22MgO-ZrO_2 thick thermal barrier coatings sprayed by atmospheric plasma spraying (APS) for diesel engine applications. Cubic zirconia peaks were detected in the as-sprayed coatings. Baig et al. [18] reported on a study of 24 MgO-ZrO_2 coatings with different architectures prepared by APS. The system they designed had a multilayer top coat that showed lower residual stress. Meanwhile, Li et al. [15] explored the behavior of APS MSZ coatings in a neutral salt spray environment.

Atmospheric plasma spraying (APS) is a thermal spray technique commonly used for producing TBC top coats. In this process, the feedstock powder enters the plasma jet where it gains thermal energy and momentum. The powder then melts and hits the substrate. Upon striking the substrate surface, the melted particles rapidly solidify, forming splats and a lamellar microstructure [1].

Flexibility in the coating microstructure can be achieved through suspension plasma spraying (SPS). Suspensions containing ultrafine particles in a dispersant medium are used as feedstock. The suspension is injected into the plasma jet where the solvent evaporates from the suspension droplets. The fine particles then agglomerate and melt as they are accelerated toward the substrate [20]. This process can produce columnar coatings with a lifetime performance comparable to that of the well-established electron beam–physical vapor deposition (EB-PVD) technique [3].

The morphology of the feedstock materials, e.g., grain size, texture, phase evolution, and stability, greatly affects the development of the coating microstructure [1]. Regarding the size of the powder particles in the suspension, particles smaller than 1 μm promote the formation of columnar structures in the deposited coatings [21]. While it is possible to achieve higher coating homogeneity by superimposing a large number of smaller lamellae, using finer powders causes poor flowability, easily clogs the injection system, and results in unstable and irreproducible feed rates [22]. These problems can be avoided by using a liquid medium to carry the fine powders, as in spraying with SPS.

Previous research has focused on optimizing the relatively new suspension plasma spray (SPS) process by controlling spray parameters, designing multilayer coatings, and pre-oxidizing the bond coat. Zhou et al. [23] compared the thermal cycling lifetime of YSZ single- and multi-layered TBCs produced by SPS and APS/SPS, respectively. Both presented extended lifetimes, with the double-layered design showing an even better result. Later, Zhou et al. [24] reported on the thermal cycling performance of single-layered (APS) and multi-layered (APS/SPS) YSZ/GZO TBCs. The multilayered TBCs exhibited significantly longer lifetimes than conventional single-layered APS-YSZ TBCs. Amer et al. [25] investigated the failure behavior of multilayered YSZ/GZO TBCs. They observed different cracking behaviors depending on the thermal treatment conditions, which can be related to stresses developed through thermal expansion mismatch and increased TGO thickness. In a recent study, Joeris et al. [26] examined the impact of controlled bond coat pre-oxidation on the performance of YSZ SPS TBCs. The lifetime of pre-oxidized coatings was longer than that of conventional TBCs. This is because the controlled bond coat pre-oxidation of the TGO reduces stresses in the topcoat.

Based on this, the aim of this study is to produce magnesia-stabilized zirconia coatings using the suspension plasma spray (SPS) technique. While MSZ coatings are already used in industry for thermal protection, this study focuses on improving coating homogeneity through the SPS technique. This work will also address the effects of multi-layered coating design and bond coat pre-oxidation on furnace cycling lifetime. Additionally, this study investigated the service life behavior of a magnesia-titania-doped zirconia system.

2. Materials and methods

2.1. Materials

The starting materials were commercial magnesia-stabilized zirconia (MSZ, 24 wt%), Metco 210NS-1, with a particle size of −90 μm/+ 11 μm, provided by Oerlikon Metco Europe GmbH; and titanium oxide (titanium(IV) oxide, anatase, 99.6 % purity) from Thermo Fisher Scientific; and a standard yttria-stabilized zirconia (YSZ, 8 wt%) powder from Oerlikon Metco, namely Metco 204NS, with a particle size range of −125/+ 11 μm.

The particle size distribution of the commercial powders was measured using the laser scattering technique with a particle size distribution analyzer (LA-950V2, Horiba). The particle distribution of the MSZ powder was d_{10} = 23.0 μm, d_{50} = 39.6 μm, and d_{90} = 65.7 μm, while the particle distribution of the TiO_2 powder was d_{10} = 0.21 μm, d_{50} = 1.25 μm, and d_{90} = 5.96 μm.

MSZ is a spheroidal powder manufactured by agglomeration and the HOSP™ process. To better understand this material, its cross section was analyzed using scanning electron microscopy (SEM) and dispersive X-ray spectroscopy (EDS). The analysis was performed using TM3000 (Hitachi) and Gemini SEM 450 (Carl Zeiss Microscopy Deutschland GmbH).

Phase composition was examined using X-ray diffraction (D4 Endeavor, Bruker).

2.2. Suspension preparation and characterization

In this study, two suspensions were prepared: one (S1) containing only MSZ particles and the other (S2) containing 7.5 TiO_2/92.5 MSZ. The only difference between the two suspensions is their composition. To produce a homogeneously dispersed suspension (30 wt% solid content in ethanol), the powders were ground in a PE bottle with a 3D shaker mixer (Turbula, WAB-GROUP), using 1.5 wt% dispersant agent (polyethylenimine, Polysciences) and 3 mm diameter alumina balls as milling media.

The particle size distribution of the suspensions was measured over

Table 1
Spray parameters for deposition of systems A, B and C.

System	Sample	APS parameters				SPS parameters				Pre-oxidation
		Topcoat Material	S (mm/s)	SD (mm)	I (A)	Topcoat Suspension	S (mm/s)	SD (mm)	I (A)	
A	MZ	MSZ	500	200	373	-				-
B	DL MZ	YSZ	500	200	420	MSZ	70	1000	220	-
	DL MZT	YSZ	500	200	420	MSZ–7.5TiO_2	70	1000	220	-
C	PO MZ	-				MSZ	70	1000	220	Argon
	PO MZT	-				MSZ–7.5TiO_2	70	1000	220	Argon

Table 2
Pretest spray conditions for APS MSZ coatings.

Pretest n.		SD (mm)	I (A)	DE (%)	Net power (kW)	Porosity (%) - examined at 500x
1	APS 1	200	420	58.8	22.7	14.6
2	APS 2	200	350	26.8	19.4	19.7
3	APS 3	250	350	16.5	18.0	20.6
4	APS 4	200	373	44.47	19.4	18.3

time, with the goal of obtaining a sub-micron particle size using the laser scattering technique with a particle size distribution analyzer (LA-950V2, Retsch Technology).

After milling, the solid load content was maintained at 5 wt% by diluting the 30 wt% suspensions in ethanol for the columnar SPS coatings. The suspensions' viscosity was measured with a viscosimeter (Physica MCR 301, Anton Paar) at shear rates between 0.1 and 1000 s^{-1} .

2.3. Coating preparation

Three different systems were designed for topcoat production, Fig. 1. System A is a single-layered APS MSZ topcoat and is used as the reference. System B is a double-layered topcoat consisting of an APS YSZ sublayer and an SPS MSZ/MSZ-Ti top layer. System C uses as-sprayed bond coat substrates that were previously oxidized and coated with an SPS MSZ/MSZ-Ti topcoat. The five coatings produced are detailed in Table 1.

The coatings were deposited onto two substrates of different materials and geometry. Stainless steel plates (25 mm×25 mm x 2 mm) were used as substrate in the pretests. The surface of the substrates was previously treated by grid blasting with Al_2O_3/F36 particles, to increase the roughness. For morphological analysis, phase identification and in the thermal cycling tests, bond coated button-shaped nickel-based superalloy – IN 738 (Ø30 mm × 3 mm) was used as substrate. The inconel substrates were provided with a NiCoCrAlHfYSi-type bond coat (Amdry 386, Oerlikon Metco), sprayed with an F4-VB torch in a LPPS/VPS facility. The bond coat layer is about 150 μm thickness. All samples were cleaned in an ultrasonic bath in ethanol prior the spray stage.

2.3.1. Processing of single-layer coatings

A single-layered APS MSZ coating, system A, was defined as the reference system. A TriplexPro™ plasma torch with a 9 mm nozzle (Oerlikon Metco), mounted on a six-axis robot in a thermal spray system Multicoat™, was used to spray the topcoat.

Based on pretests, the spray conditions were set by varying the spray distance and power to obtain coatings with a target porosity of about 18 %. Processing of the single-layered coatings was preceded by a feed rate measurement of around 34 g/min. In the preliminary tests, the parameters that were varied were the spray distance and the current, as shown in Table 2, while Ar/He ratio was maintained at 46 nlpm/4 nlpm and the robot speed at 500 mm/s.

A quantitative analysis was performed using ImageJ software to determine the overall porosity. Five cross-sectional SEM images were taken at 500x magnification for this analysis. Deposition efficiency DE (%), and net power P_{net} (kW), were calculated according to Eqs. 1 and 2, respectively.

$$DE = \frac{m_{coating \times s \times v \times \quad 60}}{n \times w \times h \; x\dot{m}_{powder}} \quad 100\% \tag{1}$$

where $m_{coating}$ is the coating mass (g); s is the meander distance (mm); v is the robot-speed (mm/s); n is the number of spray cycles; w and h, the width and length of the sample (mm), respectively; and $\dot{m}_{powder}$ is the powder mass feed rate.

$$P_{net} = L - (K \times (T_2 \quad - \quad T_1) \quad \times 4.1851 \quad \times 0.0166667) \tag{2}$$

where L is the gross power (kW); K is the waterflow (l/min); T_2 is the return temperature (°C); and T_1 is the feed temperature (°C).

2.3.2. Processing of bi-layered coatings

The YSZ sublayer of the double-layer coatings was sprayed with APS using standard methodology to produce a dense layer. After APS deposition, the average thickness of the YSZ layer was about 150 μm.

The SPS outer layer was deposited using the Axial III Torch Spray System (Northwest Mettech Corp.), which feeds the spray material axially to ensure consistent particle heating. The system was mounted on a six-axis robot. The suspension was fed using an in-house feeding system developed by Forschungszentrum Jülich. The suspension was stirred throughout the coating process to prevent line clogging and feedstock agglomeration.

The samples were sprayed with a suspension of 5 wt% MSZ or MSZ-7.5TiO_2 solids, using the following parameters: a 220 A current, a 140 V voltage, a 92.4 kW power, a 70 mm distance, a 1000 mm/s robot speed, and a calculated net power of 31.1 kW. These parameters were chosen based on preliminary tests to decrease porosity and produce a well-defined, columnar structure. The working gas was a mixture of Ar (75 vol%), H_2 (15 vol%), and N_2 (10 vol%) with a total flow rate of 245 standard liters per minute (SLPM), as described elsewhere [24,26].

The column density of SPS coatings was measured using image analysis of a cross-sectional SEM micrograph and calculated using Eq. 3. First, a straight line was drawn at the center of the topcoat. Then, the number of vertical cracks greater than half the coating thickness that intersected the line was counted [27].

$$\text{Column density} = \frac{\text{No.of column boundaries intercecting the line} - 1}{\text{True length of the line}} \tag{3}$$

2.3.3. Processing of pre-oxidized coatings

To produce coatings of system C, the bond-coated substrates were first subjected to a heat treatment in a 99.999 % pure argon atmosphere at 1 atm for two hours at 1140 °C, followed by 16 h at 870 °C, according to the parameters previously defined by Joeris et al. [26]. Then, an SPS MSZ layer of approximately 500 μm was sprayed onto the pre-oxidized substrate using the same spray conditions as those used for the aforementioned bi-layered samples.

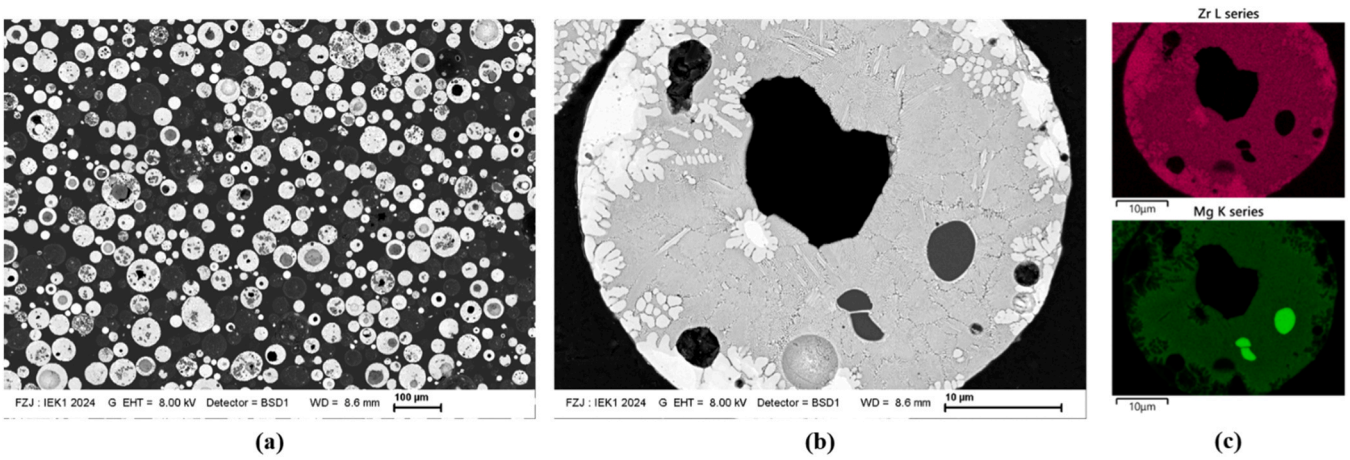

Fig. 2. (a), (b) MSZ powder cross section SEM images with two different magnifications and (c) EDX analysis.

2.4. Coating characterization

Coatings were investigated using SEM/EDS and XRD to examine morphological issues, structure, and phase composition, respectively. XRD was also used to evaluate the oxide layer of the heat-treated bond-coated substrates. Conventional metallographic techniques were used to prepare the as-sprayed samples for morphological evaluation. First, the coatings were embedded in resin and underwent a 48-hour cure. Then, they were cut using a metallographic cutting machine (Discotom-100, Struers). After that, the samples were ground and polished. The grinding steps were performed using P240–P1200 abrasive paper with 10 N of force per sample, in a clockwise direction, with water cooling, and at 150 revolutions per minute. Finally, the samples were polished with 6 µm diamond paste. The samples were cleaned with a tissue under flowing water. After cleaning with water, they were spilled with alcohol and dried. After metallographic preparation, the samples were dried in a desiccator for at least 24 h. The SEM analysis was performed using the previously described facilities. We also evaluated the presence of cracks, pores, and the thermally grown oxide (TGO) layer. The porosity level was determined via image analysis using SEM images. XRD tests were conducted on as-sprayed samples using a Malvern Panalytical Empyrean diffractometer with Cu-K_α radiation and a 2θ range of 10–90°, with a step size of 0.026°.

2.5. Furnace cycling test

Two samples of each of the five types of coatings were subjected to thermal analysis. A furnace cycling test facility was used to investigate the thermal lifetime of the as-sprayed coatings. During the tests, the samples were heated for two hours at 1100°C in synthetic air. Then, they were removed from the furnace and cooled down by a fan. They were maintained outside the furnace for 15 min. Another cycle was then repeated until failure. The samples were monitored every ten cycles, and failure was defined as spallation of approximately 20 % of the sample surface.

3. Results and discussion

3.1. Feedstock characterization

To better understand the feedstock powder, an initial characterization of the commercially available magnesia-stabilized zirconia (MSZ) was performed. Fig. 2(a) and (b) show scanning electron microscope (SEM) images of the MSZ powder cross section, which has a spherical shape with a large cavity inside, a characteristic of powders produced by the HOSP™ process. However, higher magnification and EDX analysis reveal the inhomogeneity of the powder Fig. 2(c).

Since powder morphology significantly impacts coating performance, an alternative approach was designed to obtain homogeneous MSZ coatings with full stabilization. To this end, suspensions of 30 wt% solid load of MSZ and MSZ-7.5TiO_2 were prepared for producing coatings by suspension plasma spraying (SPS). This technique produces columnar-type coatings with a much finer microstructure than conventional APS coatings, enhancing their thermo-mechanical properties [28]. Columnar coatings form due to the generation of very fine droplets during the suspension injection process. These droplets become small particles in flight once the solvent evaporates. Particles smaller than 1 µm have low momentum due to their size and exhibit a low Stokes

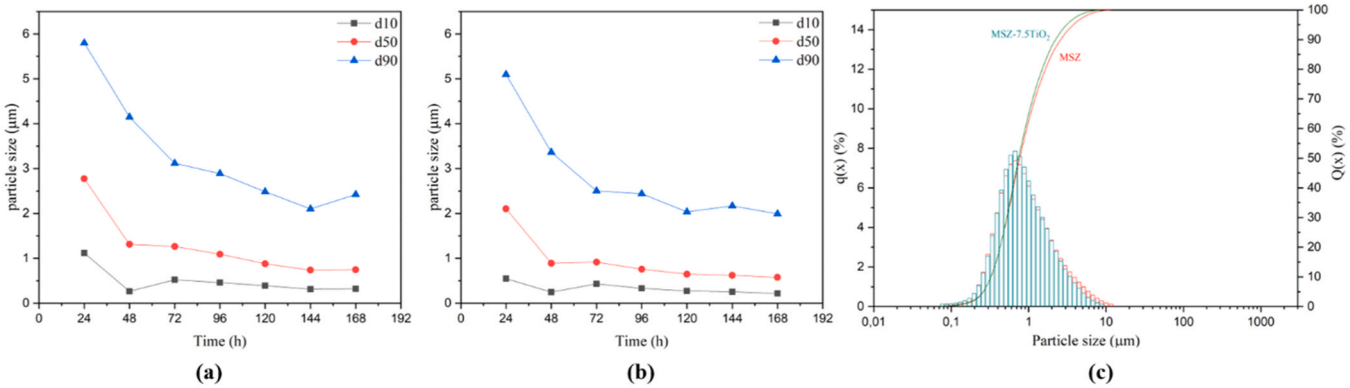

Fig. 3. Particle size distribution over time of (a) 30 % solid load suspension of MSZ in ethanol, (b) 30 % solid load suspension of MSZ-7.5TiO_2 in ethanol and (c) PSD of 5 % solid load suspensions of MSZ/MSZ-7.5TiO_2 in ethanol after 168 h milling.

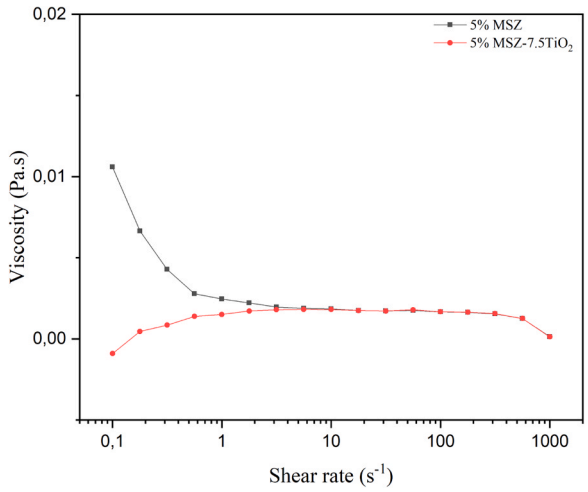

Fig. 4. Viscosity curves of MSZ/MSZ-7.5TiO_2 suspensions.

number. This makes their trajectory highly influenced by the plasma flow. Shallow impact angles and shadowing effects from surface topography contribute to the development of columnar structures in the deposited coatings [21]. Fig. 3 shows the evolution of the particle size distribution of the suspensions through ball milling until an average size below 1 μm was obtained.

The commercial MSZ powder has a large particle size (d_{50} = 39.6 μm), which requires the suspension to be milled for a long time. After 24 h of milling, the 30 % MSZ suspension had a d_{50} of 2.77 μm, as can be seen in Fig. 3(a). Since small particles tend to agglomerate and are more difficult to reduce, it was only possible to reduce the particle size below 1 μm after 120 h (d_{50} = 0.87 μm). The milling process continued for 168 h, resulting in a suspension with d_{10} = 0.30 μm, d_{50} = 0.75 μm, and d_{90} = 2.45 μm. Fig. 3(b) shows the particle size over time of the 30 % MSZ-7.5 TiO_2 solution. After 168 h of milling, the solution had a d_{10} = 0.33 μm, d_{50} = 0.84 μm, and d_{90} = 2.69 μm.

The submicron suspensions were diluted in ethanol, the distribution of which is monomodal, as seen in Fig. 3(c). The two suspensions used as feedstock for spraying consisted of MSZ and MSZ-7.5TiO2 with 5 wt% solid mass loading each. The addition of a dispersant minimized particle agglomeration.

The rheological behavior of the homemade suspensions was evaluated by measuring viscosity at different shear rates, see Fig. 4. Viscosity is the friction between successive layers of a fluid moving at different velocities. Well-dispersed and stable suspensions have low viscosity, making them easier to pump and transport. [29]. The 5 % MSZ suspensions exhibited practically Newtonian behavior. At a shear rate of 1000 s^{-1} , the viscosity of the 5 wt% MSZ and MSZ-TiO_2 suspensions was 1.34 mPa·s and 1.16 mPa·s, respectively. According to the literature, their viscosity is similar to that of a YSZ ethanol-based suspension with the same solid load content [30].

3.2. Microstructure of as-sprayed coatings

An SEM analysis was performed on a cross-section of the sample to examine its morphology and microstructure, as well as to check for cracks and pores. Porosity was also estimated via image analysis using SEM images.

3.2.1. APS MSZ coating

Various levels of porosity were achieved in the preliminary tests. When comparing coatings with the same spray distance, it was found that using lower currents in the spray process results in higher porosity. The target porosity of about 18 % was obtained by setting the spray distance to 200 mm and the current to 373 A, which were the

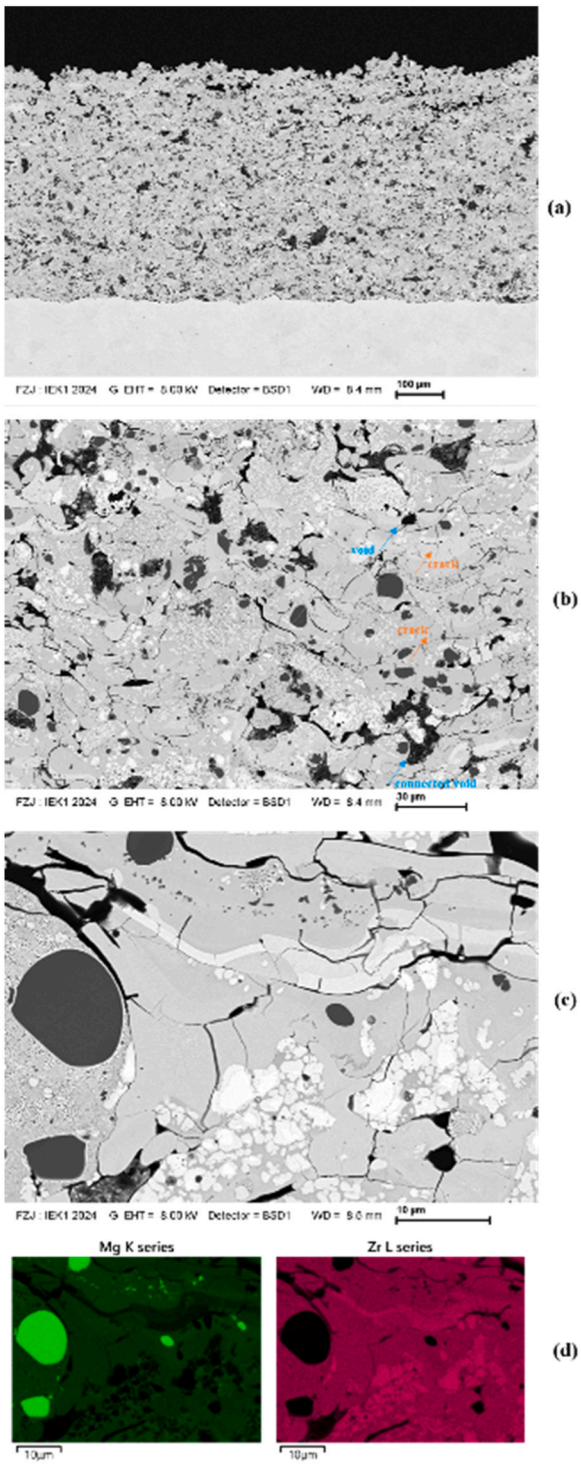

Fig. 5. MZ coating: (a) - (c) cross-sectional SEM micrographs showing microstructure in different magnifications and (d) EDX analysis.

parameters used to produce the APS single-layered coatings. This led to a deposition efficiency of around 44 % and 19 kW of net power. Generally, increasing the stand-off distance results in lower deposition efficiency because the jet cools and decelerates due to air entrapment. Conversely, increasing the current results in higher deposition efficiency [31]. Bakan et al. [32] reported on the influence of process parameters (e.g., current and stand-off distances) on porosity levels in coatings. Lower currents tend to increase porosity. Additionally, higher stand-off distances contribute to high porosity levels due to the particles' short

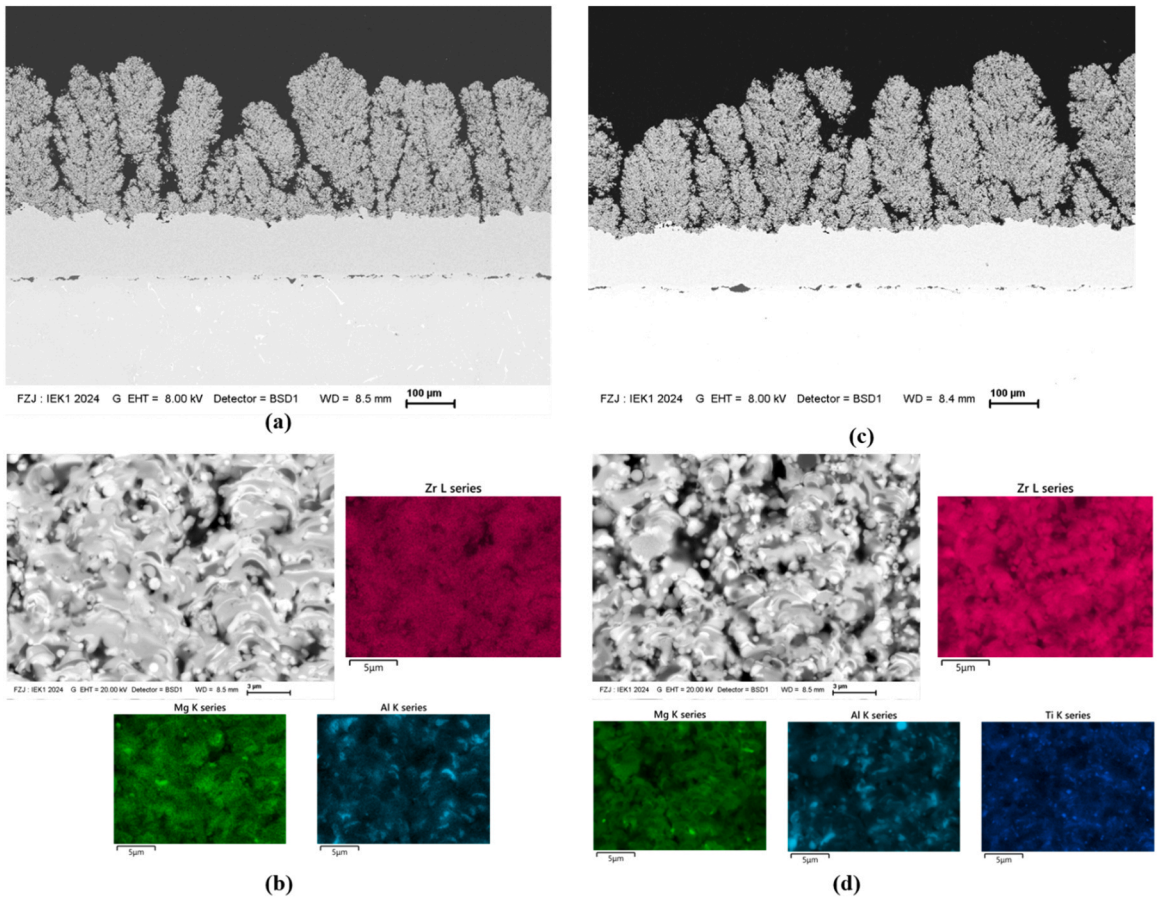

Fig. 6. (a-b) SEM micrograph and EDX mapping of a single-layered MSZ sprayed by SPS on IN738 and (c-d) SEM micrograph and EDX mapping of MSZ-7.5TiO_2 sprayed by SPS on IN738.

flight time, which results in insufficient heat transfer and incomplete melting.

Fig. 5(a-c) shows SEM images of the MSZ coating sprayed by the APS system A at different magnifications. The images reveal a lamellar morphology that is well bonded to the substrate, as well as dendritic formations similar to those observed in the original powder. Microcracks were also detected dispersed in the coating. Additionally, isolated and connected voids are present within the coating. While discrete spherical pores may decrease the coating's thermal conductivity, connected voids may increase convective heat transfer, leading to high thermal conductivity. Furthermore, cracks may accelerate spalling and lead to coating failure [33]. Fig. 5(d) shows the inhomogeneous distribution of the coating composition, as expected, since the coating microstructure is strongly influenced by the feedstock powder.

3.2.2. SPS MSZ coating

Cross-sectional images of the MSZ/MSZ-7.5TiO_2 coatings sprayed by SPS were also investigated, Fig. 6. For both compositions, the microstructure was relatively porous with a typical columnar structure, with columns separated by porous gaps that emerged from the surface. While these gaps can provide a path for hot gas and corrosive media, they also increase the top coats' strain tolerance, leading to a better thermal cycling lifetime [30]. No vertical cracks were noted in the topcoat layer. According to the literature, low-viscosity suspensions tend to produce columnar structures [34].

Elemental analysis by EDX shows homogeneous distribution of Mg, Zr, and Ti, especially in coatings prepared with an MSZ7.5TiO_2 suspension. Additionally, the addition of TiO_2 is not related to any improvement in the microstructure of the coating. Traces of Al were also noted. Debris from the alumina milling balls is an inevitable and well-known effect present in the milled powder. However, the debris is distributed so inhomogeneously that quantification by EDS was not possible. Nevertheless, we assume the amount is low because significant alumina peaks were not detected in the XRD results for the as-sprayed samples.

The column density is 11 and 8 cracks/mm for samples MSZ and MSZ-7.5TiO_2, respectively. The low values can be attributed to large column gaps and micropores inside the topcoat.

3.3. Phase characterization

XRD was used to investigate the phase characterization from the starting powder to the as-sprayed and as-cycled coatings. This included the development of the phase composition, Rietveld evaluations, and observations of how phase composition and unit cell dimensions change during cycling. The weighted profile R-factor (R_{wp}) is a measure of how well the Rietveld refinement model fits the data. In many cases, values lower than 10 % are considered acceptable [35]. The analyses in this study achieved R_{wp} values between 2 % and 6 %.

The XRD results are presented in Fig. 7, and the phase compositions are shown in Fig. 8 and summarized in Table 3.

Fig. 7(a) shows the as-received MSZ powder. The as-sprayed coatings evaluated include pre-test samples with three different APS parameters, ranging from moderate to hot (coarse particles). Finally, APS and SPS coatings (very hot and very small particles) are shown in Fig. 7(b-f). The diffractograms of the APS MSZ samples sprayed under pre-test conditions, Fig. 7(b), revealed that the APS 3 and APS 2 samples have compositions similar to the powder. Using a higher plasma power (APS 1) reduces the rhombohedral $Mg_2Zr_5O_{12}$ phase and increases the cubic $MgZr_4O_9$ phase. $Mg_2Zr_5O_{12}$ was observed to decay to $MgZr_4O_9$ and MgO

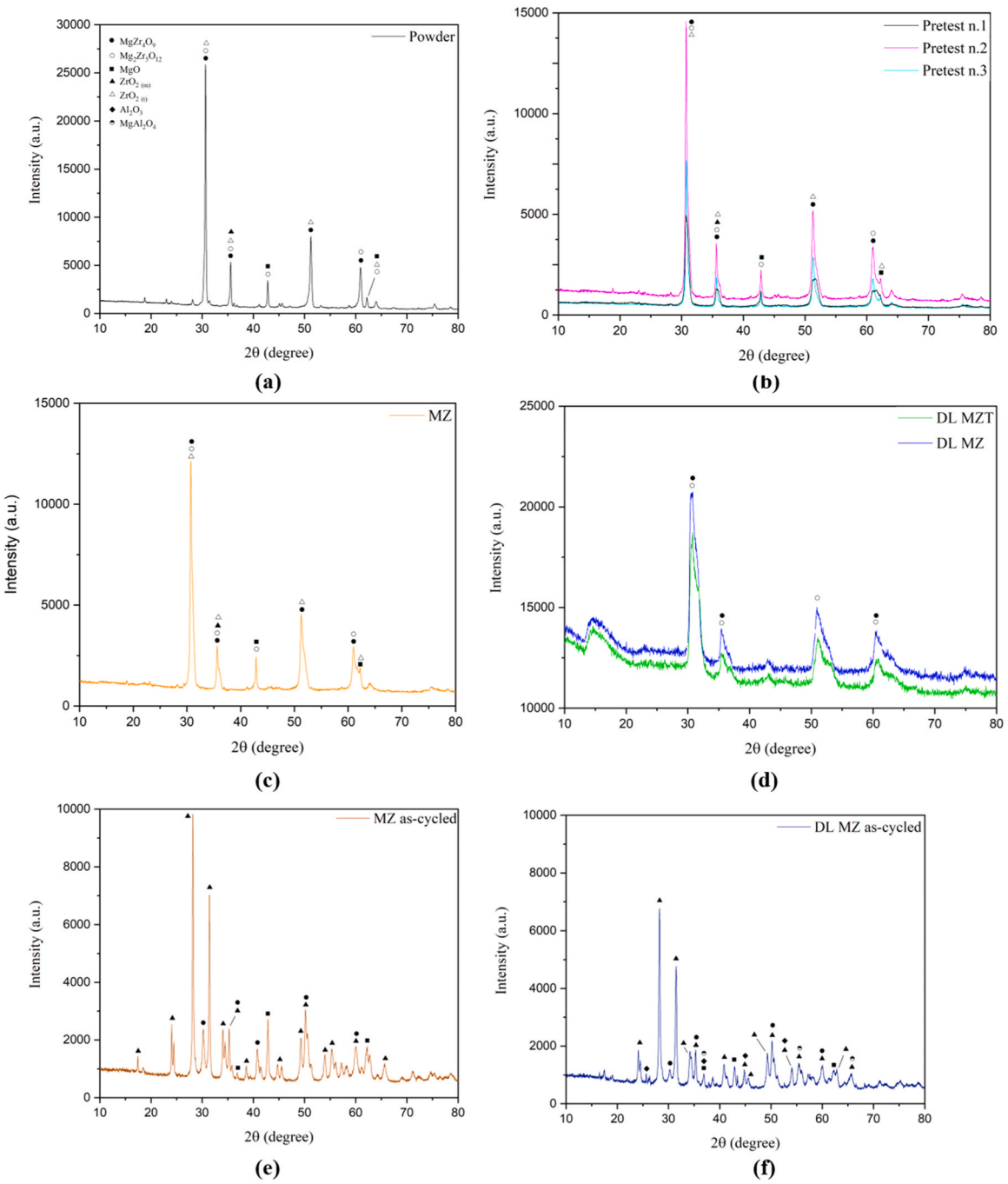

Fig. 7. XRD profile of (a) MSZ powder (b) APS MSZ pretests, (c) MZ (system A) as-sprayed, (d) DL MZ/DL MZT as-sprayed, (e) MZ (system A) as-cycled, (f) DL MZ (system B) as-cycled.

+ ZrO_2. Unstabilized monoclinic ZrO_2 disappears because it heats up during spraying and transforms into tetragonal ZrO_2 before cooling. In all cases, the molar content of MgO is similar: 89 %, 87 %, and 96 %, respectively, compared to the MgO content in the powder.

In the SPS sample, Fig. 7(d), ZrO_2 and MgO phases are absent. However, the rhombohedral $Mg_2Zr_5O_{12}$ phase and the cubic $MgZr_4O_9$ phase are present. The molar content of MgO is 39 %, which is less than half of the MgO content in the powder. This is likely due to Mg evaporation during spraying due to the solid particles' high specific surface area in the suspension and the hot conditions at SPS. Furthermore, reducing conditions due to hydrogen in the plasma gas may favor the decomposition of oxides and release of Mg, which supports the hypothesis of an inhomogeneous powder. Besides $MgZr_4O_9$ and $Mg_2Zr_5O_{12}$, there are also single oxides of Mg and Zr that could be homogenized by milling and subsequent spraying. This was not possible with the APS route. Additionally, the Ti doping is too low (7.5 wt% of the composition in a suspension with a 5 % solid load) to produce noticeable peaks. The XRD patterns of SPS MSZ and SPS MSZ-7.5TiO_2 are very similar, and distinct TiO_2-peaks are not present. The hump below 20° comes from the device.

For the as-cycled APS MSZ sample, Fig. 7(e), the calculated MgO molar content relative to the powder content was 109 %, while for the as-cycled SPS MSZ sample Fig. 7(f). it was 53 %. Within the limited accuracy of quantitative XRD analysis, these results confirm the loss of Mg in the SPS sample as opposed to the APS sample.

In XRD, the peak positions of tetragonal ZrO_2 and cubic $MgZr_4O_9$

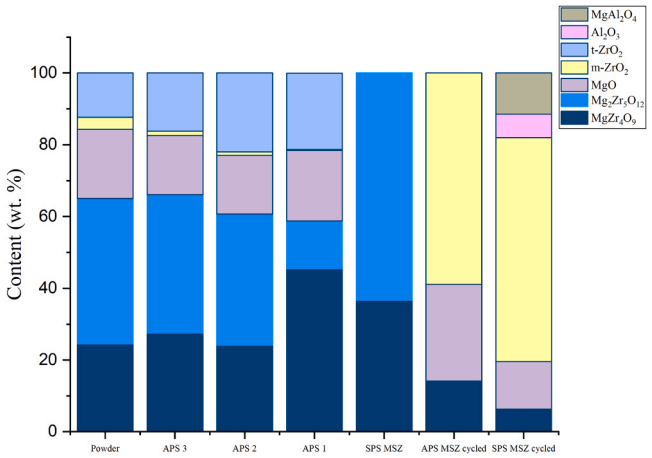

Fig. 8. Phase compositions of the feedstock powder and coatings (Pretests - APS1, APS2 and APS3; As-sprayed MSZ SPS; and As-cycled – MZ (APS MSZ) and DL MZ (SPS MSZ)).

Table 3
Phase compositions.

Phase content (wt %)	Sample						
	MSZ powder	APS 3	APS 2	APS 1	SPS MSZ	APS MSZ cycled	SPS MSZ cycled
$MgZr_4O_9$	25	28	24	45	37	14	6
$Mg_2Zr_5O_{12}$	41	39	37	13	63	0	0
MgO	19	16	16	20	0	27	13
m-ZrO_2	3	1	1	1	0	59	62
t-ZrO_2	12	16	22	21	0	0	0
Al_2O_3	0	0	0	0	0	0	7
$MgAl_2O_4$	0	0	0	0	0	0	12

overlap. Since tetragonal ZrO_2 is unlikely to exist in the cycled sample due to its metastable nature, it was omitted from the analyses. Thermal cycling transformed the rhombohedral $Mg_2Zr_5O_{12}$ phase and the cubic $MgZr_4O_9$ phase partially into MgO and unstabilized monoclinic ZrO_2. During operation at elevated temperatures, the latter transforms to tetragonal ZrO_2. This transformation is associated with a significant change in specific volume, which leads to stresses and cracks. This is believed to be the reason for the lower lifetime of the SPS samples compared to the APS samples, since the monoclinic phase forms gradually from the decay of $MgZr_4O_9$ and $Mg_2Zr_5O_{12}$ in the SPS coating. In the as-cycled SPS sample, alumina and Al-Mg spinel formed due to the diffusion of Al from the bond coat. Initially, only Al_2O_3 forms as a thermally grown oxide (TGO). Later, when aluminum is depleted in the bond coat, other oxides, such as spinels, grow quickly. Khalil et al. [36] mention that alumina can form along the bond coat interface, leading to spinel formation in the topcoat. Based on this, it is believed that the alumina peak originates from the thermally grown oxide layer on top of the bond coat.

The unit cell volumes (Å^3) of the cubic $MgZr_4O_9$ and the rhombohedral $Mg_2Zr_5O_{12}$ phases were also determined, Fig. 9(a). The unit cell volumes of $MgZr_4O_9$ and $Mg_2Zr_5O_{12}$ hardly change compared to the powder at the moderate APS 3 and APS 2 conditions. However, at the hotter APS 1 conditions, $Mg_2Zr_5O_{12}$ decomposes and more $MgZr_4O_9$ forms. This is associated with a decrease in the $MgZr_4O_9$ unit cell volume. This could be due to the formation of oxygen vacancies, resulting in a loss of specific volume. During thermal cycling, these vacancies are refilled with oxygen anions from the surrounding atmosphere. The situation is different in the as-sprayed SPS sample. Oxygen anions can transfer from $Mg_2Zr_5O_{12}$ to the presumably more stable $MgZr_4O_9$. During thermal cycling, the remaining vacancies are also filled.

Fig. 9(b) shows the combined phase content and unit cell volume data for the $MgZr_4O_9$ and $Mg_2Zr_5O_{12}$ phases. A trend can be observed: the unit cell volumes of the $MgZr_4O_9$ and $Mg_2Zr_5O_{12}$ phases evolve inversely to their contents. Oxygen vacancies may be the reason why. If one phase is present in large quantities, more oxygen vacancies are formed. One possible reason is the replacement of Zr^{4+} cations with Mg^{2+} cations, which creates oxygen vacancies in order to maintain electroneutrality. This distorts the lattice and reduces the specific volume. Since Mg is bivalent and Zr is tetravalent, when Zr^{4+} is substituted by Mg^{2+}, there is an excess of two negative elementary charges. Therefore, one O^{2-} must be removed to maintain electroneutrality. Szczerba et al. [37] reported something similar regarding the doping of zirconia with cations such as Mg^{2+}, whose ions have a size of 0.89 Å. This is related to the formation of oxygen vacancies, whereas Zr^{4+} is 0.84 Å. The removal of O^{2-} anions, which have an ionic size of 1.42 Å, should also reduce the volume of the unit cell.

Deviations from perfect crystallinity lead to the broadening of diffraction peaks. One of the main properties extracted from peak width analysis is lattice strain, which can be understood as a measure of the distribution of lattice constants arising from crystal imperfections [38]. X-ray line broadening was used to evaluate the lattice strain, and the results are provided in Fig. 9(c).

It can be observed that the lattice strain is sensitive to the spray conditions. For less power spray conditions, APS-2 and −3 (29.7 kW), there is no significative change in strain for the $MgZr_4O_9$ phase compared to the starting powder.

As can be seen, the lattice strain is sensitive to the spray conditions. For the APS-2 and −3 (29.7 kW) conditions with lower power, there is no significant change in strain for the $MgZr_4O_9$ phase compared to the initial powder.

Higher power, as observed in APS-1 (37.5 kW), increases the strain of the $MgZr_4O_9$ phase more than the $Mg_2Zr_5O_{12}$ phase. Conversely, sample SPS MSZ (sprayed with 92.4 kW of power) exhibits the largest increase in lattice strain of 194 % for the $MgZr_4O_9$ phase and 642 % for

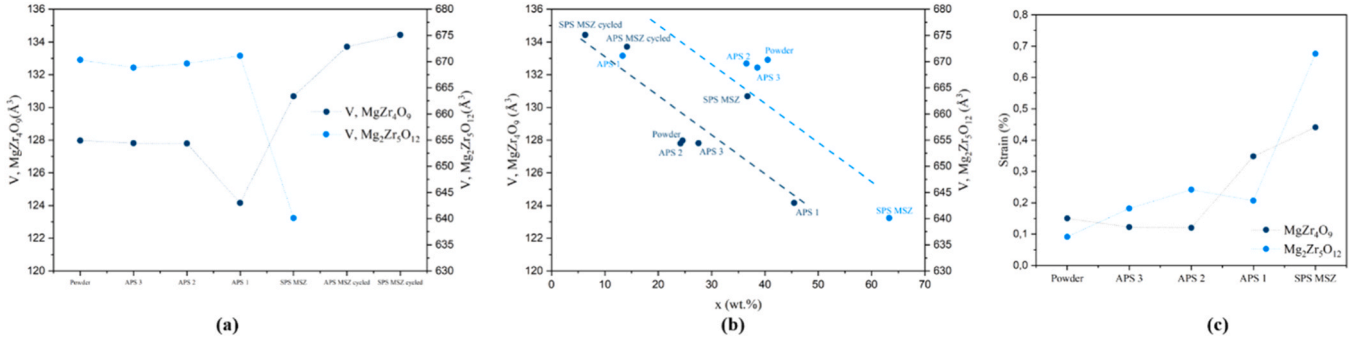

Fig. 9. (a) Unit cell volumes of the $MgZr_4O_9$ and $Mg_2Zr_5O_{12}$ phases, (b) Phase contents combined with the unit cell volumes for the $MgZr_4O_9$ and the $Mg_2Zr_5O_{12}$ phases (c) Lattice strain of the $MgZr_4O_9$ and $Mg_2Zr_5O_{12}$ phases.

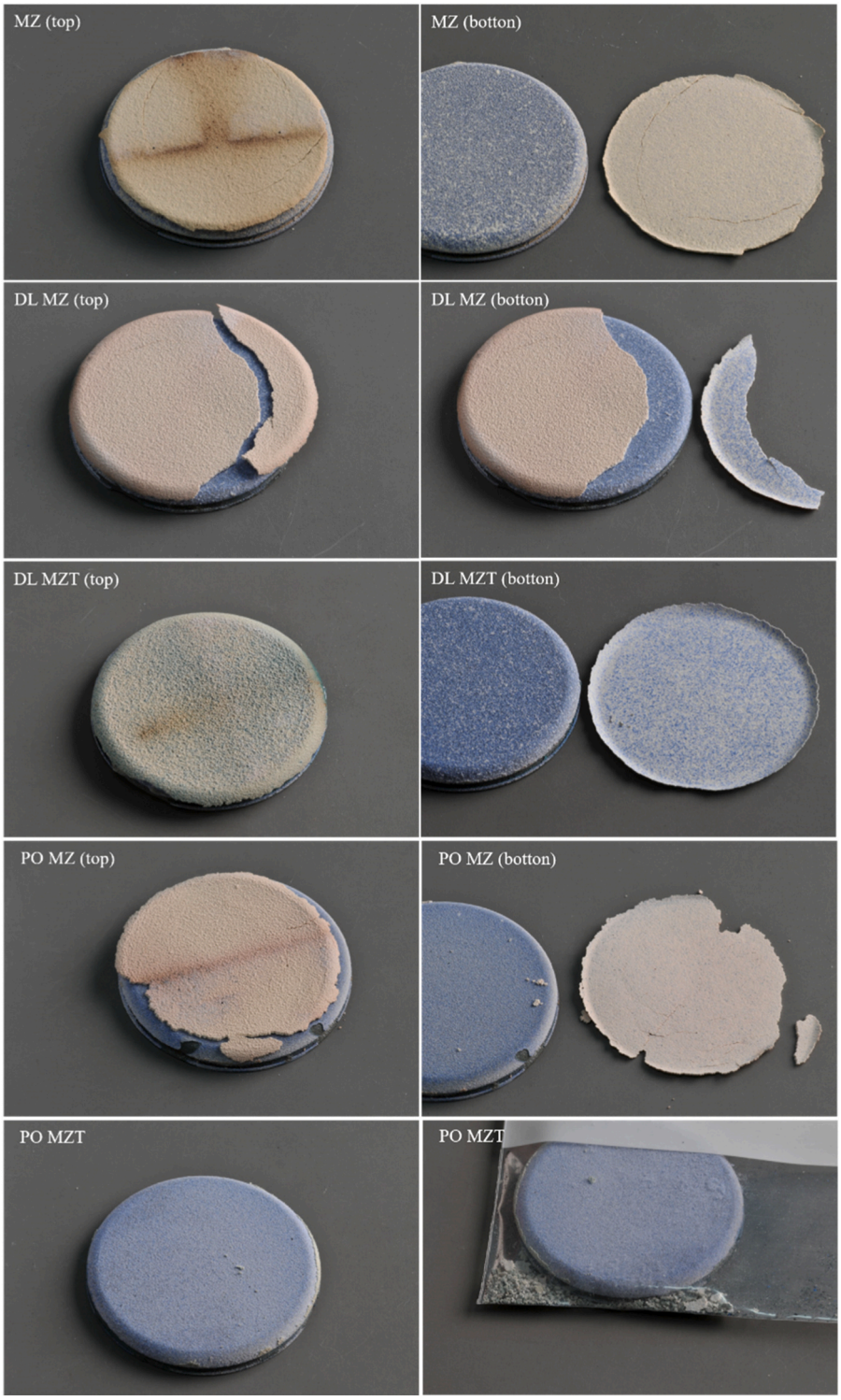

Fig. 10. Photograph of the failed TBCs after furnace cycling test.

the $Mg_2Zr_5O_{12}$ phase compared to the starting powder. This result was expected since this coating is composed solely of the $MgZr_4O_9$ and $Mg_2Zr_5O_{12}$ phases (37 and 63 wt%, respectively) and was prepared using long milling times. Ball milling is commonly used to produce fine powders from bulk materials; however, high-energy milling can induce lattice strain in crystalline particles of the material [39].

3.4. Thermal cycling performance

Fig. 10 shows photographs of the failed TBCs after thermal cycling. Table 4 summarizes the TBC lifetime for each system. During furnace cycle testing, the double-layered APS YSZ/SPS MSZ coating (system B) had a longer lifetime than the single-layered APS MSZ (system A) and pre-oxidized (system C) coatings. Since no improvement was observed with the addition of TiO_2 at the tested concentrations, no further analysis was performed.

Table 4
TBC cycle lifetime of two tested specimens.

System	Sample	1st tested specimen			2nd tested specimen		
		Thickness (μm)	Cycles to failure	Failure mode	Thickness (μm)	Cycles to failure	Failure mode
A	MZ	516	80	blue	478	80	blue
B	DL MZ	388 (243MSZ/145YSZ)	140	blue, complete spallation	398 (230MSZ/168YSZ)	140	blue, partial spallation
	DL MZT	456 (297MSZTi/159YSZ)	130	blue, complete spallation	435 (272MSZTi/163YSZ)	120	blue, complete spallation
C	PO MZ	529	80	blue, complete spallation	469	80	blue
	PO MZT	399	80	blue	379	80	blue

The APS samples were included in this study as a reference because APS is the conventional manufacturing standard for ceramic top coats on TBCs. However, it should be noted that the APS-processed coating with 373A-200mm (system A), exhibited short cycle lifetimes at 1100ºC (80 cycles). After cycling, these coatings contain a high percentage of monoclinic zirconia (59 wt%), according to Rietveld refinement analysis. This may be associated with the short coating lifetime. The APS/SPS double-layer coatings (system B) outperformed the other coatings. Both systems exhibited blue failure when the critical TGO thickness was reached, leading to spallation.

For the APS/SPS samples, failure only occurred after achieving higher lifetimes. This suggests that lower bond coat temperatures can be assumed due to the improved heat-insulating microstructure. It was noted that this coating showed spallation (partial or complete). While it was not possible to obtain long-life-cycle coatings at 1100°C, a positive trend in the processing of magnesia-stabilized zirconia coatings through SPS using an intermediate topcoat layer is evident and will require further analysis. An intermediate YSZ topcoat layer has been reported to increase the lifetime of TBCs. Zhou et al. [24] reported longer lifetimes in a burner rig test for an APS-YSZ sublayer with an SPS gadolinium zirconate (GZO) top layer compared to a typical APS-YSZ TBC. However, something similar to what Heyl et al. [40] reported could have happened in the YSZ/MSZ coatings. They studied $MgAl_2O_4$/YSZ double-layered coatings. They mention that the low toughness of the Mg-spinel layer compared to the intermediate YSZ layer might cause crack propagation close to the interface.

Additionally, peaks of alumina and spinel were observed in the topcoat X-ray diffractograms of the DL MZ sample, along with monoclinic zirconia. Different oxides form during the oxidation process. The standard free energy of formation of alumina is lower than that of other oxides, so alumina can be found at the bottom of the TGO. As the aluminum content decreases, other metal ions react with oxygen ions to form an upper-layer oxide, such as spinel [10]. However, phase transformations in the topcoat can cause additional stresses that reduce the lifetime [41].

Unexpectedly, the pre-oxidized SPS samples (system C) had lifetimes comparable to the APS reference samples. The PO MZ coating failed due to complete spallation and showed similar lifetimes (80 cycles to failure). Because the APS intermediate layer was absent, it is assumed that the adhesion strength of the SPS coating on the bond coat was insufficient to achieve the same lifetime as the double-layer systems.

The TGO layer reduces the oxidation rate by acting as a diffusion barrier for oxygen. However, TGO growth reduces the topcoat's bonding, which may result in coating failure [41]. Conversely, it is possible to extend the lifetime of coatings by pre-oxidizing the bond coat under controlled conditions. Joeris et al. [26] reported that pre-oxidizing the bond coat in argon prior to depositing the topcoat extended the lifetime of the columnar SPS coating due to changes in failure behavior. TGO growth before thermal cycling modifies the stress distribution within the coating, extending the lifetime of pre-oxidized TBCs compared to non-pre-oxidized counterparts.

4. Conclusions

This study designed and deposited different variants of magnesia-stabilized zirconia TBCs, including a single-layered reference system (APS MSZ), a double-layered system (APS YSZ/SPS MSZ), and a single-layered system (SPS MSZ) sprayed onto a pre-oxidized bond coat in argon. The microstructure, phase composition, and service life behavior were evaluated.

Reducing the input power or increasing the stand-off distance resulted in higher porosity levels in the coatings. MSZ APS TBCs with porosities of about 18 % were tested and exhibited short cycles to failure. SPS produced columnar-structured TBCs. Furnace cycling tests indicated that the APS/SPS double-layer coatings outperformed the conventional APS coatings. Unexpectedly, the pre-oxidized SPS samples had lifetimes comparable to those of the APS reference system. Thus, it is assumed that the multilayer coating has better adhesion strength. Titania doping with a content of 7.5 wt% was not to be beneficial in terms of coating lifetime.

SPS is considered a promising technology for optimizing the processing of MSZ coatings to increase their service point, which is currently around 900°C. Future experiments must clarify the failure mechanisms, which may be associated with phase transformations and compound formation.

CRediT authorship contribution statement

B.S. Constantino: Conceptualization; Data curation; Formal analysis; Investigation; Methodology; Writing - original draft. **Y.J. Sohn:** Formal analysis; Investigation. **G. Mauer:** Formal analysis; Methodology; Supervision; Validation; and Writing - review & editing.

Declaration of Competing Interest

The authors declare that they have no known competing financial interests or personal relationships that could have appeared to influence the work reported in this paper.

Acknowledgments

This study was funded by the Deutscher Akademischer Austauschdienst (DAAD) through the Research Stays for University Academics and Scientists Program, grant no. 91782186. Thanks also go to Sigrid Schwartz-Lückge for her help preparing the suspensions, to Frank Kurze and Karl-Heinz Rauwald for their help with the spraying, to Dr. Daniel E. Mack and Martin Tandler for their help with the thermal cycling tests, to Dr. Doris Sebold for her help with the microscopy tests, to Michel Xhonneux for his help with the metallography, and to Andrea Hilgers for her help with the suspension-related tests. The first author would also like to thank her colleagues, Dr. Dapeng Zhou and Dr. Jana Joeris, for their help interpreting the results, as well as Maheshwar Bagathi and Dr. Edward J. Gildersleeve, for discussing the operation of the spray facilities.

References

[1] P.G. Lashmi, P.V. Ananthapadmanabhan, G. Unnikrishnan, S.T. Aruna, Present status and future prospects of plasma sprayed multilayered thermal barrier coating systems, J. Eur. Ceram. Soc. 40 (2020) 2731–2745, https://doi.org/10.1016/j.jeurceramsoc.2020.03.016.

[2] E.J. Gildersleeve, R. Vaßen, Thermally sprayed functional coatings and multilayers: a selection of historical applications and potential pathways for future innovation, J. Therm. Spray. Tech. 32 (2023) 778–817, https://doi.org/10.1007/s11666-023-01587-1.

[3] R. Vaßen, E. Bakan, Daniel E. Mack, Olivier Guillon, A perspective on thermally sprayed thermal barrier coatings: current status and trends, J. Therm. Spray. Tech. 31 (2022) 685–698, https://doi.org/10.1007/s11666-022-01330-2.

[4] M.R. Dorfman, G. Dwivedi, C. Dambra, S. Wilson, Perspective: challenges in the aerospace marketplace and growth opportunities for thermal spray, J. Therm. Spray. Tech. 31 (2022) 672–684, https://doi.org/10.1007/s11666-022-01351-x.

[5] E.J. Gildersleeve, V. Viswanathan, S. Sampath, Molten silicate interactions with plasma sprayed thermal barrier coatings: role of materials and microstructure, J. Eur. Ceram. Soc. 39 (2019) 2122–2131, https://doi.org/10.1016/j.jeurceramsoc.2019.01.023.

[6] V. Viswanathan, G. Dwivedi, S. Sampath, Multilayer, multimaterial thermal barrier coating systems: design, synthesis, and performance assessment, J. Am. Ceram. Soc. 98 (2015) 1769–1777, https://doi.org/10.1111/jace.13563.

[7] H. Cai, X. Shan, J. Lu, L. Luo, Z. Cai, W. Wang, X. Zhang, X. Zhao, The crack behavior and delamination mechanisms of air plasma sprayed thermal barrier coatings under ultrasonic plasma jet at 1600 °C, J. Eur. Ceram. Soc. 43 (2023) 4136–4145, https://doi.org/10.1016/j.jeurceramsoc.2023.03.005.

[8] S. Mahade, D. Zhou, N. Curry, N. Markocsan, P. Nylén, R. Vaßen, Tailored microstructures of gadolinium zirconate/YSZ multi-layered thermal barrier coatings produced by suspension plasma spray: durability and erosion testing, J. Mater. Process Technol. 264 (2019) 283–294, https://doi.org/10.1016/j.jmatprotec.2018.09.016.

[9] K. Leng, A. Rincon Romero, T. Hussain, Multilayer GZ/YSZ thermal barrier coating from suspension and solution precursor thermal spray, J. Eur. Ceram. Soc. (2023), https://doi.org/10.1016/j.jeurceramsoc.2023.04.014.

[10] Y. Zhao, Y. Ge, X. Jin, D. Koch, R. Vaßen, Y. Chen, X. Fan, Oxidation behavior of double-ceramic-layer thermal barrier coatings deposited by atmospheric plasma spraying and suspension plasma spraying, Ceram. Int 48 (2022) 23938–23945, https://doi.org/10.1016/j.ceramint.2022.05.068.

[11] G. Chen, Q. Li, Y. Ling, H. Zheng, J. Chen, Q. Jiang, K. Li, J. Peng, M. Omran, L. Gao, Phase stability and microstructure morphology of microwave-sintered magnesia-partially stabilised zirconia, Ceram. Int 47 (2021) 4076–4082, https://doi.org/10.1016/j.ceramint.2020.09.281.

[12] Y. Wu, Y. Wang, E.J. Gildersleeve V, P.F. Hsu, S. Sampath, M.H. McCay, Laser thermal gradient testing of air plasma sprayed multilayered, multi-material thermal barrier coatings, Int J. Appl. Ceram. Technol. 19 (2022) 2632–2647, https://doi.org/10.1111/ijac.14100.

[13] J. Cho, B. Yang, C. Shen, H. Wang, X. Zhang, Micromechanical properties and microstructure evolution of magnesia partially stabilized zirconia prepared by spark plasma sintering, J. Eur. Ceram. Soc. 43 (2023) 1098–1107, https://doi.org/10.1016/j.jeurceramsoc.2022.10.021.

[14] J. Wang, J. Sun, Q. Jing, B. Liu, H. Zhang, Y. Yongsheng, J. Yuan, S. Dong, X. Zhou, X. Cao, Phase stability and thermo-physical properties of ZrO2-CeO2-TiO2 ceramics for thermal barrier coatings, J. Eur. Ceram. Soc. 38 (2018) 2841–2850, https://doi.org/10.1016/j.jeurceramsoc.2018.02.019.

[15] Z. Li, H. Wu, Y. Bai, D. Cong, A. Huang, K. Song, M. Zhang, Z. Wei, X. Ding, X. Wang, D. Peng, Study on damage behavior of NiCoCrAlY/MSZ Plasma-Sprayed coating in neutral salt spray environment, Coatings 12 (2022), https://doi.org/10.3390/coatings12111611.

[16] T.A. Schaedler, R.M. Leckie, S. Krämer, A.G. Evans, C.G. Levi, Toughening of nontransformable t′-YSZ by addition of titania, J. Am. Ceram. Soc. 90 (2007) 3896–3901, https://doi.org/10.1111/j.1551-2916.2007.01990.x.

[17] J.A. Krogstad, M. Lepple, C.G. Levi, Opportunities for improved TBC durability in the CeO2-TiO2-ZrO2 system, Surf. Coat. Technol. 221 (2013) 44–52, https://doi.org/10.1016/j.surfcoat.2013.01.026.

[18] M.N. Baig, F.A. Khalid, F.N. Khan, K. Rehman, Properties and residual stress distribution of plasma sprayed magnesia stabilized zirconia thermal barrier coatings, Ceram. Int 40 (2014) 4853–4868, https://doi.org/10.1016/j.ceramint.2013.09.035.

[19] S. Ahmaniemi, J. Tuominen, P. Vuoristo, T. Mä, Sealing procedures for thick thermal barrier coatings, J. Therm. Spray. Tech. 11 (2002) 320–332.

[20] F. Curà, R. Sesana, L. Corsaro, R. Mantoan, Characterization of thermal barrier coatings using an active thermography approach, Ceramics 5 (2022) 848–861, https://doi.org/10.3390/ceramics5040062.

[21] N. Curry, K. VanEvery, T. Snyder, J. Susnjar, S. Bjorklund, Performance testing of suspension plasma sprayed thermal barrier coatings produced with varied suspension parameters, Coatings 5 (2015) 338–356, https://doi.org/10.3390/coatings5030338.

[22] A. Joulia, G. Bolelli, E. Gualtieri, L. Lusvarghi, S. Valeri, M. Vardelle, S. Rossignol, A. Vardelle, Comparing the deposition mechanisms in suspension plasma spray (SPS) and solution precursor plasma spray (SPPS) deposition of yttria-stabilised zirconia (YSZ), J. Eur. Ceram. Soc. 34 (2014) 3925–3940, https://doi.org/10.1016/j.jeurceramsoc.2014.05.024.

[23] D. Zhou, D.E. Mack, P. Gerald, O. Guillon, R. Vaßen, Architecture designs for extending thermal cycling lifetime of suspension plasma sprayed thermal barrier coatings, Ceram. Int 45 (2019) 18471–18479, https://doi.org/10.1016/j.ceramint.2019.06.065.

[24] D. Zhou, D.E. Mack, E. Bakan, G. Mauer, D. Sebold, O. Guillon, R. Vaßen, Thermal cycling performances of multilayered yttria-stabilized zirconia/gadolinium zirconate thermal barrier coatings, J. Am. Ceram. Soc. 103 (2020) 2048–2061, https://doi.org/10.1111/jace.16862.

[25] M. Amer, N. Curry, Q. Hayat, R. Sharma, V. Janik, X. Zhang, J. Nottingham, M. Bai, Cracking behavior of Gd2Zr2O7/YSZ multi-layered thermal barrier coatings deposited by suspension plasma spray, Coatings 13 (2023), https://doi.org/10.3390/coatings13010107.

[26] J. Joeris, W.S. Scheld, S. Uhlenbruck, Y.J. Sohn, D. Sebold, O. Guillon, R. Vaßen, Preparation of highly durable columnar suspension plasma spray (SPS) coatings by Pre-Oxidation of the CoNiCrAlY bond coat, Coatings 13 (2023), https://doi.org/10.3390/coatings13091575.

[27] N. Kumar, M. Gupta, Daniel, E. Mack, G. Mauer, Robert Vaßen, Columnar thermal barrier coatings produced by different thermal spray processes, J. Therm. Spray. Tech. 30 (2021) 1437–1452, https://doi.org/10.1007/s11666-021-01228-5.

[28] E. Rosado, E. Cañas, P. Recio, E. Sánchez, R. Moreno, ZrSiO4/ZrO2 thermal barrier coatings produced by suspension plasma spraying, J. Eur. Ceram. Soc. 44 (2024) 460–470, https://doi.org/10.1016/j.jeurceramsoc.2023.09.024.

[29] L. Pawlowski, Suspension and solution thermal spray coatings, Surf. Coat. Technol. 203 (2009) 2807–2829, https://doi.org/10.1016/j.surfcoat.2009.03.005.

[30] D. Zhou, O. Guillon, R. Vaßen, Development of YSZ thermal barrier coatings using axial suspension plasma spraying, Coatings 7 (2017), https://doi.org/10.3390/coatings7080120.

[31] R. Vaßen, T. Kalfhaus, C. Vorkötter, Y.J. Sohn, S. Conze, Lutz, M. Berger, Atmospheric plasma spraying of different MgO/Al 2 o 3 feedstocks, J. Therm. Spray. Tech. 32 (2023) 514–522, https://doi.org/10.1007/s11666-023-01541-1.

[32] E. Bakan, D.E. Mack, G. Mauer, R. Vaßen, Gadolinium zirconate/YSZ thermal barrier coatings: plasma spraying, microstructure, and thermal cycling behavior, J. Am. Ceram. Soc. 97 (2014) 4045–4051, https://doi.org/10.1111/jace.13204.

[33] Y. Huang, X. Song, C. Lin, W. Zheng, Yi Zeng, J. Huang, Unveiling of lanthanum-yttrium co-doped zirconia and yttrium-stabilized zirconia calcium-magnesium-alumina-silicate corrosion behavior, J. Therm. Spray. Tech. 32 (2023) 59–71, https://doi.org/10.1007/s11666-022-01498-7.

[34] F. Tarasi, E. Alebrahim, A. Dolatabadi, C. Moreau, A comparative study of YSZ suspensions and coatings, Coatings 9 (2019), https://doi.org/10.3390/COATINGS9030188.

[35] R.A. Young (Ed.), The Rietveld Method, Oxford University Press, 1993.

[36] M.A.E. Hafez, S.A. Akila, M.A. Khedr, A.S. Khalil, Improving wear resistance of plasma-sprayed calcia and magnesia-stabilized zirconia mixed coating: roles of phase stability and microstructure, Sci. Rep. 10 (2020), https://doi.org/10.1038/s41598-020-78088-6.

[37] K. Wisniewska, D. Madej, J. Szczerba, The corrosion of Mg-partially stabilized zirconia during service in continuous casting tundish, J. Ceram. Sci. Technol. 9 (2018) 301–308, https://doi.org/10.4416/JCST2018-00019.

[38] P. Bindu, S. Thomas, Estimation of lattice strain in ZnO nanoparticles: X-ray peak profile analysis, J. Theor. Appl. Phys. 8 (2014) 123–134, https://doi.org/10.1007/s40094-014-0141-9.

[39] H. Heyl, D.E. Mack, M. Tandler, S. Schrüfer, R. Vaßen, Effects of laser-structured and APS flash-coated CoNiCrAlY bond coats on the furnace cycle lifetime of double-layered Y2O3-stabilized ZrO2/MgAl2O4 abradable coatings, Surf. Coat. Technol. 464 (2023), https://doi.org/10.1016/j.surfcoat.2023.129513.

[40] A.A. Al-Tabbakh, N. Karatepe, A.B. Al-Zubaidi, A. Benchaabane, N.B. Mahmood, Crystallite size and lattice strain of lithiated spinel material for rechargeable battery by X-ray diffraction peak-broadening analysis, Int. J. Energy Res. 43 (2019) 1903–1911, https://doi.org/10.1002/er.4390.

[41] C. Vorkötter, D.E. Mack, O. Guillon, R. Vaßen, Superior cyclic life of thermal barrier coatings with advanced bond coats on single-crystal superalloys, Surf. Coat. Technol. 361 (2019) 150–158, https://doi.org/10.1016/j.surfcoat.2019.01.001.